RESEARCH ARTICLE

ADVANCED
SENSOR
RESEARCH
Open Access

www.advsensorres.com

Check for updates

Optimization of Transcutaneous Oxygenation Wearable Sensors for Clinical Applications

Juan Pedro Cascales,* Emmanuel Roussakis, Matthias Müller, Lilian Witthauer, Xiaolei Li, Avery Goss, Helen Keshishian, Haley L. Marks, John Q. Nguyen, Liv Kelley, and Conor L. Evans*

Abstract: In this manuscript, the development of an experimental and mathematical toolset is reported that allows for improved *in vivo* measurements of optical transcutaneous oxygen tension measurements (TCOM) wearable technology in humans. In addition to optimizing O_2-sensing films for higher sensitivity oxygen detection, calibration algorithms are additionally developed to account for excitation source leakage, as well as algorithms to combine readings of partial pressure of oxygen (pO_2), derived from phosphorescence intensity and lifetime, into a single metric. This new iteration of the TCOM wearable device is then tested in a pilot human study. By implementing characterization and calibration algorithms, the data from the pilot study demonstrates the ability to obtain reliable transcutaneous pO_2 readings with a TCOM sensor regardless of size and without the need for strict conditions of constant temperature, humidity, or motion that have limited the range of applications of this technology in the past.

1. Introduction

The ability to quantitatively determine oxygen concentration in living tissue can be decisive for diagnosing and treating a number of conditions. While clinical tools based on blood oxygen saturation are widespread, these devices do not provide a direct measure of oxygen concentration and can fall short in scenarios where no blood flow or the presence of blood pooling, such as in ischemic injury, diabetic ulcers,[1] tourniquet application, and skin burn treatments[2,3] and exercise monitoring.[4] In these cases, direct measurement of tissue oxygen concentration via non-invasive approaches such as *transcutaneous oxygen tension measurement (TCOM)* can be advantageous. However, current clinical TCOM technologies are limited in part, due to their cost, large physical size, and cumbersome operation. Additionally, these devices generally require constant and fixed conditions to yield reliable measurements, such as long calibration procedures or equilibration times,[5–7] or operating temperature requirements of over 40°C.[8] These restrictive conditions impede the use of current TCOM systems, for example, to monitor preterm neonates, as they can obtain electrode-induced burns due to elevated measurement temperatures.[7,9]

There are several techniques capable of producing TCOM sensors, including the electrochemical Clark electrode,[10] photoacoustic detection,[11–13] or the use of metalloporphyrin molecules that undergo phosphorescence quenching in the presence of oxygen.[14,15] Of these various techniques, optical sensing tools based on porphyrins have shown the most promise in producing miniaturized and user-friendly devices. The phosphorescence quenching of these molecules is oxygen dependent and follows the Stern-Volmer relation:[16]

$$\frac{\tau_0}{\tau} = 1 + K_{SV} \cdot pO_2 \tag{1}$$

with τ as the lifetime at a given partial pressure of oxygen or pO_2, τ_0 as the lifetime in the absence of oxygen, and K_{SV} as the Stern-Volmer quenching constant. In terms of an oxygen sensitive porphyrin, both τ and τ_0 can be replaced with the porphyrin's phosphorescence, I and I_0, respectively.,

Commercial efforts have been successful in producing oxygen sensing devices, which had wearable components but were not fully non-invasive.[17–20] Promising current research involves the use of low-power electronics, with the proposed

J. P. Cascales, E. Roussakis, M. Müller, L. Witthauer[+], X. Li, A. Goss, H. Keshishian, H. L. Marks, J. Q. Nguyen, L. Kelley, C. L. Evans
Wellman Center for Photomedicine, Massachusetts General Hospital
Harvard Medical School
Boston, MA USA
E-mail: jcascalessandoval@mgh.harvard.edu;
evans.conor@mgh.harvard.edu

J. P. Cascales
Departamento de Química en Ciencias Farmacéuticas, Facultad de Farmacia
Universidad Complutense de Madrid
Plaza Ramón y Cajal S/N, Madrid 28040, Spain

**ADVANCED
SCIENCE NEWS**

www.advancedsciencenews.com

**ADVANCED
SENSOR
RESEARCH**
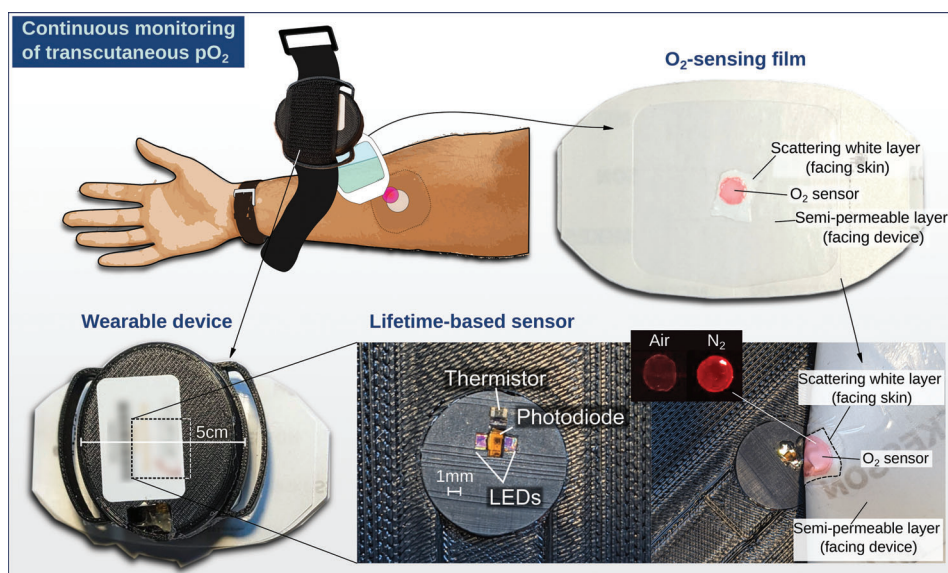
Open Access

www.advsensorres.com

Figure 1. Diagram illustrating use of the TCOM wearable. The small and lightweight device probes the phosphorescence lifetime of the oxygen-sensitive metalloporphyrins via surface mounted electronics (two excitation LEDs and a PIN photodiode). The multilayer film is composed of medical grade adhesive, a polymer film with the embedded porphyrins, and a breathable scattering layer for optical insulation and increasing the phosphorescence signal collected by the detector. The films are pre-attached to the device and then applied to the skin for probing tissue oxygenation.

devices being based on both intensity of lifetime, although more work is required to optimize the ergonomics and portability of the devices.[21–26] Recently, we reported on the first fully self-contained wearable *transcutaneous* oxygen sensor.[27,28] The simplicity of the device was possible due to the use of an ultrabright porphyrin molecule[29] that produces long-lasting phosphorescence ($\approx 10 - 100\mu s$) detectable with commodity electronic hardware. Devices utilizing pO_2 sensors based on phosphorescence lifetime[27] offered reliable measurements that exhibit reduced influence from photobleaching, film positioning, and motion artifacts. Additionally, the oxygen sensing film formulations were formulated to be humidity insensitive,[30] which was found crucial for skin wearable devices as relative humidity can widely vary depending on the device's location on the body. Despite their success, these initial developments led to devices that had moderate sensitivity to oxygen due to both sensor and hardware limitations that required challenging calibration and analysis procedures.

In this manuscript, we detail the development of experimental and mathematical characterization techniques that further optimize the previously developed TCOM wearable technology for human applications without compromising the current compact and straightforward device design. Specifically, we introduce a novel iteration of our TCOM wearable that utilizes optimized films for improved sensitivity to O_2. Additionally, we have also developed new calibration algorithms to address excitation source leakage along with algorithms for integrating multiple pO_2 readings into a single metric. Lastly, we present the initial proof-of-principle measurements using this improved approach obtained from a pilot study conducted with healthy human subjects.

2. Experimental Section

The oxygen-sensing technology presented in Ref. [27] had been optimized for use in humans. This had been achieved by reduc-

ing and compensating for excitation source leakage, tailoring the dye concentration and device sensitivity to work in the relevant pO_2 range of interest and by tuning and characterizing the oxygen diffusion properties of the O_2-sensing films.

As seen in **Figure 1**, the wearable devices were small and light, with prototypes weighing around 30 grams. As was described in Ref. [27], the heart of the device consists on custom electronics (a fast ADC chip, transimpedance amplifier and signal conditioning block) built around a wireless-capable microcontroller board (Particle Photon). The printed circuit boards (PCBs) had been redesigned to improve signal-to-noise and to use an LED modulation frequency of 1.6kHz, as previous versions used 796Hz.[27] The change in modulation frequency allows for a more accurate determination of lifetime (and therefore of pO_2) from fitting a sum of sinusoids to the signals, as the change in observed phase was a larger proportion of an oscillation period. The phosphorescence lifetime of the medical-grade adhesive oxygen sensing film was probed via two excitation high-power UVA LEDs (385nm), a PIN photodiode and a temperature sensor. The LED emission was filtered by a 400 nm short-pass filter composed of two ultra-thin flexible optical notch-filters. The LED emission was blocked by placing a 500 nm long-pass filter over the PIN photodiode, by combining a flexible 405 nm long-pass filter and a polyamide film. The oxygen sensing film was composed of: a semi-permeable transparent membrane partially occluding the skin from atmospheric oxygen, a thin poly(propyl methacrylate) (PPMA) layer with the embedded metalloporphyrins, a transparent and breathable membrane and a spin coated, white scattering breathable layer serving as optical insulation. Tissue oxygenation readings were obtained by pre-attaching a film to the device using double-sided adhesive, and then applying the films to the skin. To ensure a proper seal against the skin and prevent the device from detaching, the device was secured onto the subject under study with an elastic velcro band.

2.1. Signal and Film Optimization

A key factor limiting the sensitivity of our device was the LED emission leaking into the photodiode signal. As both LEDs and photodiode were on the same plane, the main contribution of this leakage to come from the sides was identified. This unwanted cross-talk was blocked by physically separating the photodiode from the LEDs with a thin and opaque (black) plastic layer or by filling the space with black nail polish (Ted Pella, Inc. from Fisher Scientific), as can be seen in the sensor head close-up in Figure 1.

Without unwanted LED light saturating the photodiode signal, and with feedback from our first testing in humans (reported below), it was possible to increase the dye concentration by a factor of three (from $30\mu M$ up to $90\mu M$), and to increase the gain of the trasimpedance amplifier by a factor of four with respect to the previous device,[27] which makes full use of the analog-to-digital converter's (ADC) range in the pO_2 range of interest, between 60 and 160 mmHg, which was found to be optimal for transcutaneous measurements on healthy human subjects. Reducing LED leakage also allowed to increase the modulation frequency, which was set at $f = 1.6kHz$, which corresponds to the optimal modulation frequency[31] for a lifetime of $\tau \approx 100\mu s$. These changes yield measurements with improved signal-to-noise ratio (SNR) (see Table S2, Supporting Information).

With input from the human pilot studies, it was found necessary to reduce the influence of atmospheric oxygen in order to obtain a better sensitivity to physiological changes in oxygenation. This could be achieved by using a less breathable polyurethane (PU), semi-permeable layer to block out more atmospheric pO_2. The original $30\mu m$ film (Tegaderm 1626W, 3M) was replaced by a thicker $50\mu m$ film (Bioclusive, McKesson).

The difference in response was tested by carrying out a calibration with the described oxygen-sensing film structure employing thin and thick PU dressings. The films were placed over a custom made flow-cell in which the oxygen concentration was varied from 160 mmHg down to 0 mmHg and up to 160 mmHg again via a gas mixer combining N_2 and air at different ratios. The phosphorescence lifetime was measured using an Edinburgh Instruments FLS1000 spectrometer. The film created a seal over the flow-cell such that one side of the film was exposed to atmospheric oxygen (imaging side) while the other (O_2-sensor side) was exposed to the variable atmosphere in the flow-cell, similarly as when the films are used for in vivo measurements. The lifetime values versus flow-cell pO_2 are shown in **Figure 2a**, which present a larger change in lifetime for the thick film because more atmospheric oxygen was prevented from entering the multilayer compared to the thin one.

As was discussed in previous work,[32] the measurement of oxygen concentration was obtained from porphyrins that were embedded in a polymer film, which was sandwiched between two other layers, and hence not in direct contact with the patient's skin. Therefore, there was an oxygen gradient through the film between atmosphere on one side and skin pO_2 on the other (or flow-cell pO_2 in this experiment), so the devices provide pO_2 readings, which were at an intermediate concentration. The reduced inflow of oxygen from the atmo-
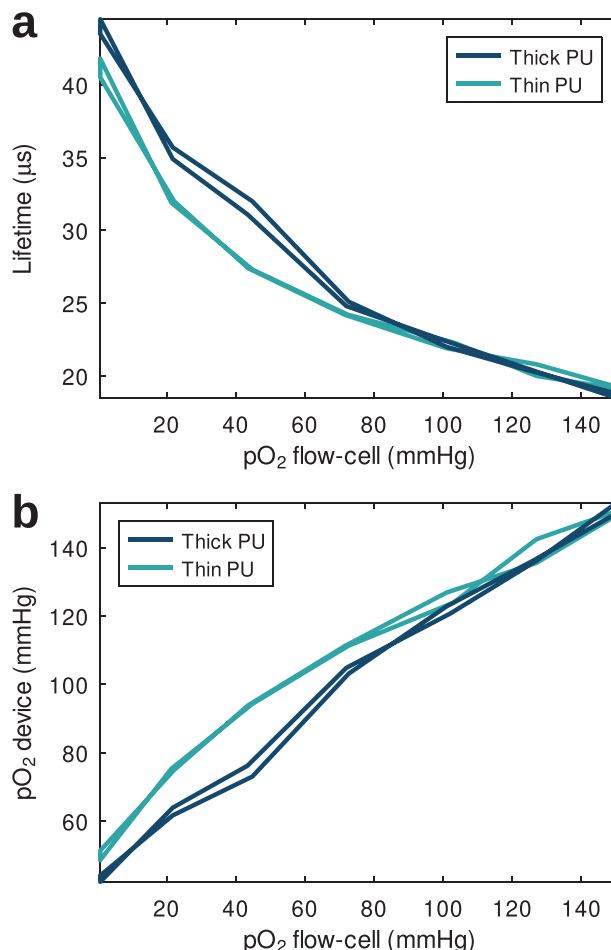

Figure 2. a) Dependence of phosphorescence lifetime with oxygen partial pressure two polyurethane medical dressings of different thickness, 30 and 50 μm. The measurement is taken using a flow cell in which the films are exposed to the pO_2 values shown in the x-axis on the bottom and atmospheric oxygen on the top. The thicker polyurethane membrane blocks atmospheric oxygen so the oxygen-sensing layer equilibrates down to lower pO_2 (longer lifetime) values. b) Sensor pO_2 (calculated from lifetime) versus flow-cell pO_2, with the thicker dressing showing a smaller difference with respect to the oxygenation at the bottom of the O_2-sensing film.

sphere results in the oxygen-sensing film equilibrating down to a pO_2 value closer to the tissue's. The true tissue oxygenation could be calculated by characterizing the diffusivity of the film's layers and inverse boundary problem using differential equations.[32]

In order to quantify the difference between bottom (flow-cell or tissue when in vivo) pO_2 and the oxygenation measured by the device, sensor pO_2 was estimated (Figure 2b). $\tau_0 = 96\mu s$ and $K_{SV} = 0.27 mmHg^{-1}$ was used, which was calculated from the Stern-Volmer equation and using the lifetime values in atmospheric conditions from Figure 1a. The result of a linear fit ($pO_2^{sensor} = m \cdot pO_2^{flow-cell} + b$) for $pO_2^{flow-cell} > 40 mmHg$ yields $m = 0.7$ and $b = 48 mmHg$ for the thick PU layer and $m = 0.5$ and $b = 72 mmHg$ for the thin film, which supported the increased sensitivity in vivo using films employing a thicker PU layer.

ADVANCED
SCIENCE NEWS

www.advancedsciencenews.com
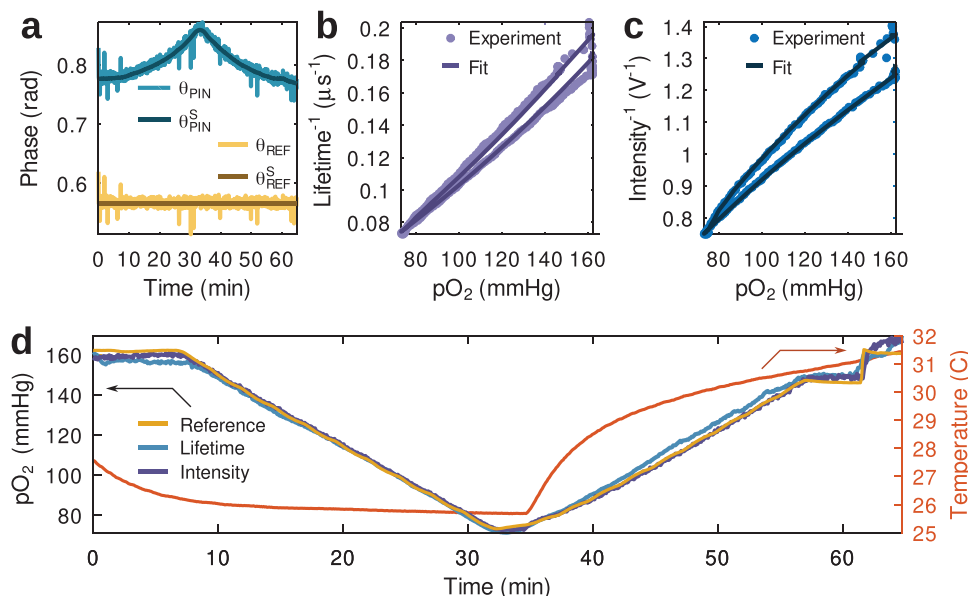
ADVANCED
SENSOR
RESEARCH

www.advsensorres.com

Figure 3. Calibration algorithm taking into account LED leakage. a) Smoothing of the LED driving signal's (reference signal) and photodiode signal's phase by subtracting the fluctuations in the reference signal phase from both. Fits of the b) *lifetime* and c) *intensity* data to the calibration algorithm. The model is able to describe the variation of the measured lifetime and intensity in relation to changes in pO_2 and temperature. d) The phosphorescence lifetime and intensity derived pO_2 shows a good agreement with the commercial pO_2 sensor (left axis), throughout the temperature range shown in the graph (right axis).

3. Results

3.1. Signal Processing

Oxygen sensing via phosphorescence lifetime detection utilizes a 1.6 kHz sinusoidal reference signal that drives a set of UV excitation LEDs,[27] with phase and amplitude that are dependent on oxygen following the Stern–Volmer relation.[16] A multiple linear regression model is fit to both the voltage signal driving the LEDs and the photodiode's signal, to extract the phase θ_{REF} of the reference and θ of the phosphorescence signals along with the phosphorescence intensity I. In our previous work, the relative phase $\theta_{REF} - \theta$ was used as the oxygen-dependent parameter, as it is related to the lifetime τ of the emission. The pO_2 estimate derived from lifetime (pO_2^τ) can be more robust against photobleaching and motion artifacts when compared to that obtained from intensity (pO_2^I).

However, if a small amount of LED light leaks through the optical filters and into the PIN photodiode, then the detected signal is a combination of the porphyrin's phosphorescence signal plus a small contribution from the excitation LEDs, both due to relative LED/photodiode placement and non-ideal emission/collection optical filters. In addition LEDs, in particular ultraviolet emitting LEDs, often suffer from visible and near-infrared luminescence emission that, while weak, can be strong enough to spectrally interfere the oxygen-sensitive emission of the porphyrin molecule.[27] This translates to the phase θ having a slight intensity dependence and therefore not being fully insensitive to photobleaching or motion. Here, we propose the following calibration algorithm in order to account and compensate for the LED leakage in these devices.

3.1.1. Removing the Effect of LED Leakage

The novel LED leakage calibration requires the use of parameters θ_{REF} and θ rather than their relative changes to calibrate and extract the proper phosphorescence lifetime. To remove the phase fluctuations shown in **Figure 3a** that arise from the microcontroller clock and trigger time of each pO_2 measurement, we calculate the mean value of θ_{REF}, label it as θ_{REF}^S, and use it from now on as the reference signal's phase. The fluctuations $\Delta\theta_{REF} = \theta_{REF} - \theta_{REF}^S$ are removed from the photodiode phase by $\theta^S = \theta - \Delta\theta_{REF}$, which is from now on referred to as the photodiode phase.

The combination of emitter and detector placement, optical filters, and optical masks help to remove most of the unwanted LED emission from the measured signal. However, it is possible to still observe that some amount of the final signal is due to the LED when using blank multilayer films that do not contain porphyrins. In this section, we aim to computationally remove the contribution of the LEDs to the measured phosphorescence signal. The model assumes the sine wave is a sum of two components, LED and porphyrin, and we are able to obtain only the contribution to the signal coming from the porphyrin, therefore "removing" the LED contribution to the original signal measured by the photodiode.

The phosphorescence signal is a sinusoid at $f = 1.6$ kHz, which we define as $\gamma(t) = I\cos(\omega t + \theta)$, with $\omega = 2\pi f$, and I being the amplitude and θ being the phase obtained from the photodiode's signal. We know that a sum of sinusoids with the same frequency but different phase and amplitude, can be expressed as a *single* sinusoid at that frequency with some phase and amplitude[33] (see Supporting Information for proof).

**ADVANCED
SCIENCE NEWS**

www.advancedsciencenews.com

**ADVANCED
SENSOR
RESEARCH**
Open Access

www.advsensorres.com

Therefore, if we suppose that $\gamma(t)$ is the sum of two sinusoids corresponding to the LED leakage and the porphyrin signals, we have:

$$\gamma(t) = I \cos(\omega t + \theta) = A \cos(\omega t + \alpha) + B \cos(\omega t + \beta) \tag{2}$$

with (A, α) and (B, β) being the amplitude and phase of the LED leakage and of the porphyrin, respectively.

Again using the property stated above for a sum of sinuoids of the same frequency,[33] the following equations hold:

$$I \cos\theta = A \cos\alpha + B \cos\beta = x \tag{3}$$

$$I \sin\theta = A \sin\alpha + B \sin\beta = y \tag{4}$$

where I and θ can be calculated by:

$$I = \sqrt{x^2 + y^2} \tag{5}$$

$$\theta = \arctan\left(\frac{y}{x}\right) \tag{6}$$

The calibration algorithm consists of simultaneously minimizing Equations (3) and (4), employing calibration data from the TCOM device's response and an oxygen commercial sensor. The different coefficients are dependent on pO_2 and temperature as described below.

The LED amplitude A measured with a blank film (no embedded porphyrin) was found to depend linearly with temperature in the range of 20–40°C. We define the temperature T_0 to be 32° (typical skin temperature), A_0 as the LED amplitude at T_0 and A_1 the change in LED amplitude per degree. Therefore, we express the LED's temperature dependence as:

$$A = A_0 \cdot (1 - A_1(T - T_0)) \tag{7}$$

The LED's signal phase α is assumed to be equal to θ_{REF} (i.e., the LED's driving signal) plus an added phase α_0 that can be due to a delay in the LED's response with respect to the driving signal. Additionally, as was discussed in Ref. [27], the UVA LEDs used in the TCOM device exhibit wide phosphorescence signals that overlap in wavelength with the emission of the oxygen sensing porphyrin that can also contribute to α_0. The final equation is:

$$\alpha = \theta_{REF} + \alpha_0 \tag{8}$$

The porphyrin signal's amplitude B depends on an oxygen-dependent intensity B_{SV} and is also directly proportional to the LED excitation A:

$$B = B_{SV} \cdot A \tag{9}$$

It can be seen from this equation and Equarions (6) and (7) that the temperature dependence of the LED cancels out from the measured phase θ. The phosphorescence intensity B_{SV} depends on oxygen following the Stern-Volmer relation:

$$B_{SV} = \frac{I_0}{(1 + K_{SV} \cdot pO_2)} + I_{OFF} \tag{10}$$

with I_0 the intensity in the absence of oxygen and I_{OFF} an intensity offset that we attribute to a small fraction of porphyrin molecules that can be shielded from oxygen by the polymer film.[27,34] The quenching constant K_{SV} has a linear dependence with temperature[27]

$$K_{SV} = K_0 + K_1(T - T_0) \tag{11}$$

The porphyrin's phase β will be the sum of α plus the added delay due to the phosphorescence signal β_{SV}:

$$\beta = \beta_{SV} + \alpha \tag{12}$$

In turn, β_{SV} depends on the lifetime τ and modulation frequency f:

$$\tan\beta_{SV} = 2\pi f\tau \tag{13}$$

Lifetime τ depends on oxygen following the Stern-Volmer relation:

$$\tau = \frac{\tau_0}{(1 + K_{SV} \cdot pO_2)} + \tau_{OFF} \tag{14}$$

with τ_0 the lifetime in the absence of oxygen, experimentally determined as $\tau_0 = 96\mu s$,[27] and a lifetime offset τ_{OFF} again attributed to shielded porphyrin molecules. K_{SV} values are the same as for intensity.

3.1.2. Estimating pO_2 from the Fitting Coefficients

The non-linear fitting function yields values for the following fitting coefficients $[K_0, K_1, I_0, I_{OFF}, \tau_{OFF}, A_0, A_1, \alpha_0]$. The offsets I_{OFF}, τ_{OFF} are small compared to I_0, τ_0 (2% and 3%, respectively) and can be set to zero. Estimates of pO_2 from phosphorescence lifetime (pO_2^τ) and intensity (pO_2^I) can be then obtained from the fitting coefficients and the experimentally obtained I and θ.

Lifetime-derived pO_2.
Using Equations (3) and (4), we can write:

$$W = \tan\beta = \frac{sin\beta}{cos\beta} = \frac{I \sin\theta - A \sin\alpha}{I \cos\theta = A \cos\alpha} \rightarrow \beta$$

$$= \arctan(W) \rightarrow \beta_{SV} = \beta - \alpha \rightarrow \tau = \frac{\tan\beta_{SV}}{2\pi f} \tag{15}$$

Then, this estimated τ can be substituted in Equation (14) to produce:

$$pO_2^\tau = \frac{1}{K_{SV}}\left(\frac{\tau_0}{\tau - \tau_{OFF}} - 1\right) \tag{16}$$

Intensity-derived pO_2.
From Equations (4) and (7), we can calculate B_{SV} as follows:

$$B = \frac{I \cos\theta - A \cos\alpha}{cos\beta} = B_{SV} \cdot A \rightarrow B_{SV} = \frac{I \cos\theta - A \cos\alpha}{A \cos\beta} \tag{17}$$

**ADVANCED
SCIENCE NEWS**

www.advancedsciencenews.com

**ADVANCED
SENSOR
RESEARCH**

www.advsensorres.com

Then, the calculated B_{SV} can be substituted in Equation (10) as for lifetime:

$$pO_2^I = \frac{1}{K_{SV}} \left(\frac{I_0}{B_{SV} - I_{OFF}} - 1 \right) \tag{18}$$

Figure 3b–d shows the fitting of the described algorithm to data obtained during a calibration. The algorithm was implemented in GNU Octave[35] and the fitting was carried out using a non-linear least squares data solver. The calibrations were carried out in a sealed calibration chamber in which the temperature and pO_2 can be controlled by a hot plate and by varying the mix of nitrogen and air gas being fed into a programmable gas mixer (Gometrics, Spain).[36] The partial oxygen pressure in the chamber was measured with a commercial oxygen sensor (PreSens, Regensburg, Germany).

Figure 3b,c illustrates how alterations in pO_2 and temperature result in discernible patterns within the lifetime and intensity data. These patterns are effectively captured by the fitting algorithm. Further, the assessment of pO_2 derived from both lifetime and intensity data, as shown in Figure 3d, closely match the measurement from the commercial pO_2 sensor. The model, therefore, allows us to estimate the phosphorescence lifetime of our oxygen sensors reliably, providing a pO_2 dependent metric, which is independent of intensity.

The fitting parameters such as K_0, K_1, which are indicative of the breathability of the films, yield values in agreement with those previously found.[27,34,37] We found that K_0 and K_1 exhibit consistent values throughout the different films and can be made into a fixed value by calculating the mean value obtained from calibrating multiple films with one device ($\approx 7 \cdot 10^{-2}$mmHg^{-1} and $\approx 2 \cdot 10^{-3}$mmHg$^{-1}C^{-1}$, respectively). Additionally, the LED intensity leaking into the detector A_0 matches what is observed with blank films containing no porphyrin. Finally, the phase offset in the LED phase α_0 can also be made a fixed value as it is defined by the electronic circuit ($2.5 \cdot 10^{-1}$rad for the device discussed here).

3.1.3. Combining Phosphorescence Lifetime and Intensity Into a Unified pO_2 Metric

The oxygen sensing device can produce two pO_2 estimates each with their own advantages and disadvantages: one derived from phosphorescence lifetime and one from intensity.[27] The metric derived from lifetime (pO_2^τ) is quantitatively accurate as it is more robust against motion, film positioning, and photobleaching. However, it presents lower SNRs that could potentially lead to the missed detection of small, but crucial physiological, changes in oxygenation, especially at higher partial pressures. On the other hand, pO_2 derived from intensity (pO_2^I) presents higher SNRs and can detect changes in oxygenation with high sensitivity over a wider range of pressures, but can have stray readings values due to the effects of changes in the film's positioning or photobleaching related to dye concentration.

One possible way of taking advantage of both metrics is to combine the best features of each into a single optimized pO_2 metric. Ideally, we would like to keep the reliable mean value (low frequencies representing the slow trend from pO_2^τ lifetime), while adding the low noise and fast changes (high frequencies) seen in pO_2^I.

To do this, we use the Fast Fourier Transfrom (FFT) along with its respective low and high pass filters to extract the high (phosphorescence intensity) and low (phosphorescence lifetime) frequency features of each of the pO_2 estimates before combining them with weights A_τ, A_I to produce a single frequency domain representation. Calculating the inverse FFT gives us the combined pO_2 measurement.

$$pO_2 = ifft\{A_\tau \cdot LP \cdot fft(pO_2^\tau) + A_I \cdot HP \cdot fft(pO_2^I)\} \tag{19}$$

Several potential functions were tested and evaluated. We used a nonlinear fitting algorithm with each of the functions to obtain the fitting coefficients (A_τ, A_I weights, cut-off frequency, filter order, etc.) that produce the best fit of each of the algorithms to the ideal pO_2 by combining pO_2^τ and pO_2^I.

The first function tested was the ideal frequency-domain low pass filter, which is a rectangular or brick-wall filter given by:

$$H_{BW}(f) = \begin{cases} 0, & \text{if}|f| > f_c, \\ 1/2, & \text{if}|f| = f_c, \\ 1, & \text{if}|f| < f_c \end{cases} \tag{20}$$

with f_c as the cutoff frequency. The function H_{BW} corresponds to a low pass filter, to produce a high pass filter, the $<$ should be exchanged with $>$ and vice versa. To obtain the optimal combined pO_2, the non-linear fit was carried out using f_c, A_τ and A_I as fitting coefficients.

Because the sharpness of the brick-wall filter in the frequency domain can result in ringing in the time domain due to the filter corresponding to a *sinc* function in the time domain, we alternatively tested other continuous or smooth functions to perform the low and high pass filtering. One such example is the Butterworth filter:

$$H_{BU}(f) = \frac{1}{\sqrt{1 + (|f|/f_c)^{2n}}} \tag{21}$$

This filter can (numerically) be used as a high pass filter by a $y - axis$ reflection at $f/f_c = 1$. The variable coefficients are f_c, filter order n_τ and n_I, A_τ. and A_I.

The third filter tested was the Fermi filter, which is a step-like function:

$$H_{Fermi}(f) = \frac{1}{e^{((|f|-f_c)/C)} + 1} \tag{22}$$

The main advantage of this filter is that it can be continuously tuned from a brick-wall filter into a step function with a smooth transition by tuning the constant C, and can used as a high pass filter by inverting the sign of $(|f| - f_c)$. The fitting coefficients were f_c, C_{LP}, C_{HP}, A_τ, and A_I.

Lastly, we used the Kalman filter, which is widely used to obtain smooth estimates of signals given input from multiple noisy sensors and is therefore a natural choice for our purpose. As input for the Kalman filter, we calculate the standard deviation of pO_2^τ and pO_2^I along with the moving standard deviation over a sliding window of 6 points (equivalent to 30s of data with $\Delta t = 5$s). There are three fitting coefficients: the state transition model value, and the two diagonal elements of the observation model matrix.

**ADVANCED
SCIENCE NEWS**

www.advancedsciencenews.com

**ADVANCED
SENSOR
RESEARCH**
Open Access

www.advsensorres.com

To test these algorithms, we created synthetic numerical pO_2 data mimicking our clinical trial results (see Supporting Information), which are shown in **Figure 4**. Creating our own data (with features similar to those seen in the human measurements) allows for control over the reading's magnitude and noise, as well as show the different features observed in the clinical measurements: an initial period sampling atmospheric oxygen, an exponential decrease to an equilibrium value upon application of the device on skin, a sine-like oscillation (representing blood flow occlusion), and an exponential return to atmospheric oxygen seen when the device is removed from skin. It also allows us to define a desired *ideal* combination of intensity and lifetime metrics and to accurately gauge the difference between the ideal response and the fit of each filter. Lifetime measurements (yellow curve in **Figure 5**) are assumed to be close in value to the true oxygen partial pressure (gray curve in Figure 5), but present higher noise, which can obscure the fast subtle changes in oxygen due to events such as an occlusion. Intensity readings (red curve in Figure 5) may stray from the true pO_2 but present low noise and respond sharply to physiological changes in oxygenation. Our aim is therefore to combine the lifetime (yellow) and intensity (red) curves and get as close as possible to an ideal reading (gray).

The results in Figure 5 show the combined pO_2 metric plotted along with the lifetime, intensity and ideal pO_2 curves in order of quality of the fit (black line).

The mean residual and SNR of the best-fit combined pO_2 for each filter type is shown in Figure 5e. We obtained the R^2 parameter (or goodness of fit) by:

$$R^2 = 1 - Var(y - y_{fit})/Var(y) \tag{23}$$

and the SNR in decibels (dB) by:

$$SNR_{dB} = 10 \cdot log_{10}[R^2/(1 - R^2)] \tag{24}$$

As can be seen Figure 3, as well as in Figure 5a–d, the Fermi filter produces the fit with with lowest residual (i.e., closest to the ideal pO_2 reading), as well as the highest SNR, meaning it is the most effective at combining the desired features from the lifetime and intensity pO_2 readings. The brickwall filter is close in fit quality to the Fermi filter, and we attribute the difference between them to tunability of the smoothness of the step transition of the Fermi filter, which prevents ringing effects in the time-domain and may allow contributions slightly above and below the cut-off frequency.

3.2. Pilot Study

As mentioned earlier, improvements in materials, device and data processing were iteratively improved and validated through a pilot study. Institutional Review Board (IRB) approval was granted under Partners Healthcare (MGH) under protocol number 2019P001637. For the study, healthy adult subjects were recruited without giving preference to any particular age, sex, or skin tone (Fitzpatrick skin phototype), and those with preexisting skin conditions were excluded. The measurements were carried out according to the following protocol:

i) Initially, the device probes atmospheric pO_2 for around 10 min. *ii)* For an optimal measurement, the area of skin to which the wearable was attached was cleaned with isopropanol and the superficial layer of the stratum corneum was exfoliated by stripping the skin ten times with medical tape.[5] The device was then applied to a subject's inner forearm as shown in **Figure 4a** and allowed to equilibrate for ≈30 min. *iii)* A change in tissue oxygenation was induced using blood pressure cuffs or tourniquets applied to the extremities. After the amount of pressure applied reaches 250 mmHg or 75 mmHg above their systolic blood pressure, no more pressure was applied for 3 to 6 min, after which, the pressure was released, and the output of the device was recorded for an additional 30 min.

A total of four subjects were measured, and the results are summarized in Figure 4b. Subjects #1 and #3 opted for the pressure cuff, while #2 and #4 chose the tourniquet, which produced a more apparent response. The graphs show the gradual improvement in signals due to changes in the film and device discussed above, with the last measurement achieving the cleanest signal and reaching a lower equilibrium pO_2. It should be noted that not all differences between the different subjects were due to the materials and device, but could also be due to difference between subjects, such as differences in the subject's skin thickness, blood circulation, metabolism, amount of muscle under the skin, thickness or absence of fatty tissue between the skin and muscle, etc. These could limit the application of transcutaneous oxygen sensors in general to some patients. Other contributions to the differences between measurements could be due to the fact that our films are stacked by hand, and there could be inter-film differences such as trapped pockets of air between the layers, as well as the application by hand of the adhesive film, which can produce different wrinkles with each subject upon sealing over the skin due to hair, morphology, etc.

In order to compare the change in oxygenation measured for all subjects, the exponentially decaying background observed (Figure 4b) in the readings upon application of the device to the skin was removed by fitting and subtracting an exponential function from the measurements. This exponentially decaying signal is due to the diffusion of oxygen through the film, which takes place because each side of the film experiences a different oxygen concentration (one side atmosphere, the other skin pO_2).[32] The background-subtracted results are shown in Figure 4c, with the last measurement showing the largest change in oxygenation due to the occlusion and clearly shows the expected trend of decreasing oxygenation upon cuffing, subsequent increase, and overshoot upon release of the tourniquet (reactive hyperemia), and return to the initial pO_2 value.

4. Conclusion

This manuscript presents a comprehensive approach to fully exploit the potential of optical TCOM wearable technology for measuring transcutaneous partial pressure of oxygen (pO_2) in humans. The device and analysis methods have been optimized to minimize LED leakage into the photodetector, which in turn, allows us to maximize the measured phosphorescence signal. We introduced a new calibration scheme, which aims to remove the effect of residual excitation LED leakage, resulting in a lifetime estimate, which is independent of excitation intensity. From a manufacturing point of view, this calibration algorithm also has the advantage of reducing the need for using high-quality
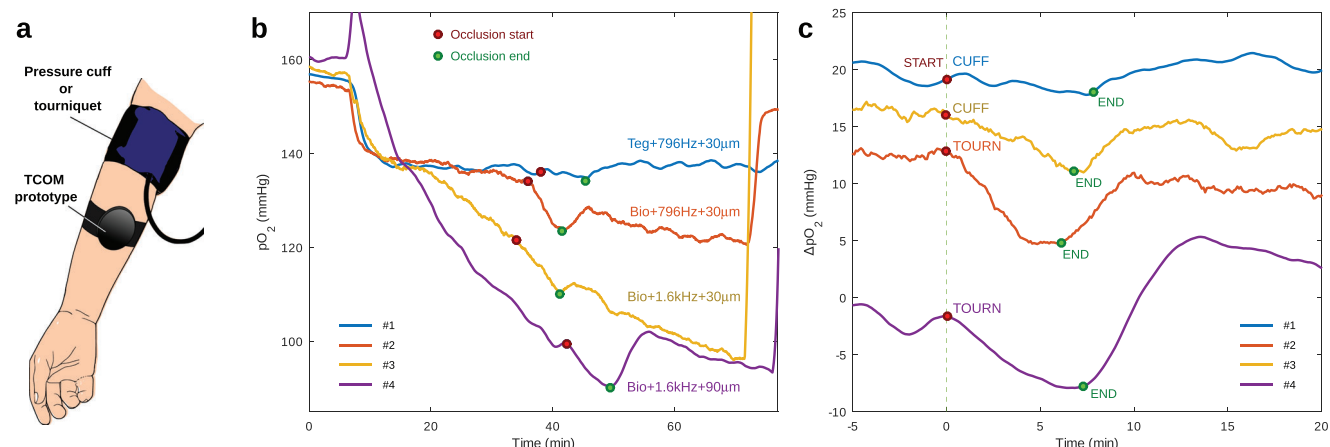
Figure 4. Pilot study with the TCOM wearable. (a) The TCOM device is applied to the inner forearm and blood flow is restricted via a blood pressure cuff or emergency tourniquet. (b) Testing of the different configurations of device and films measuring pO_2 on 4 study subjects, showing a gradual improvement as the equilibrium pO_2 reaches lower values and the changes in transcutaneous oxygenation become more apparent. (c) Change in the oxygenation due to the occlusion of blood flow. Measurement #4 shows the largest change in oxygenation due to the occlusion, with decreasing oxygenation upon cuffing, and the expected increase and overshoot upon release of the tourniquet. The exponentially decaying background was removed for comparison of the values.
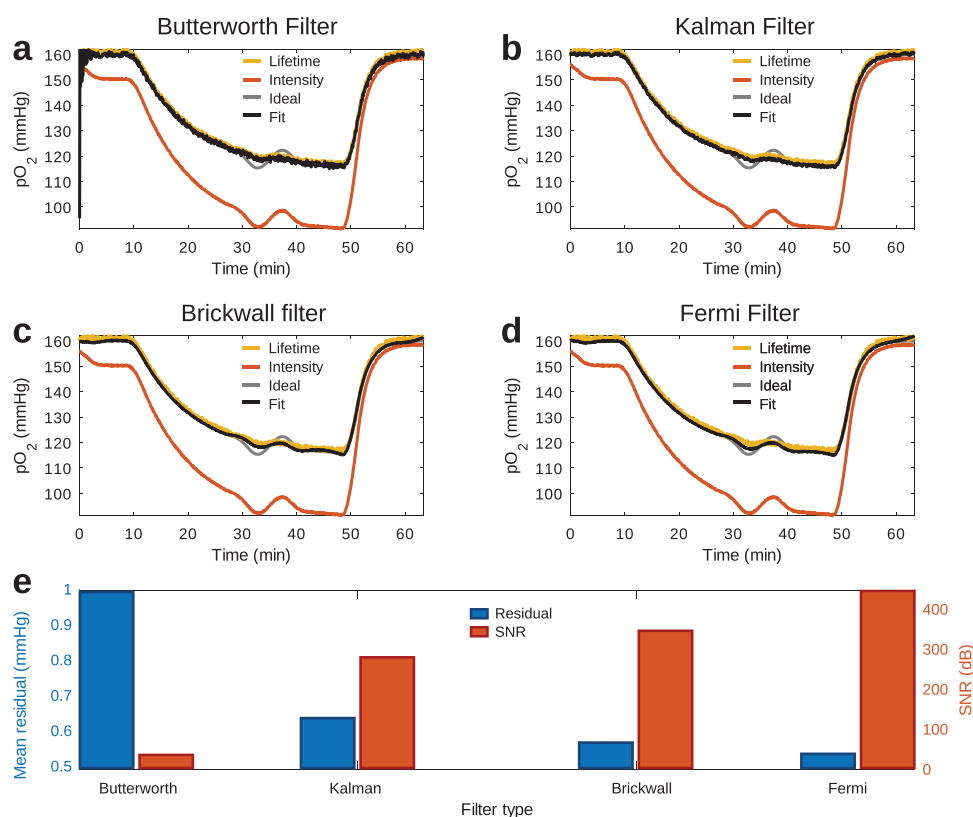

Figure 5. Synthetic pO_2 measurements mimicking readings on humans with a 20 min equilibration time and a 5 min occlusion. The best fit to the ideal pO_2 reading is obtained by combining pO_2 readings derived from lifetime and intensity using the following filters: a) Butterworth filter, b) Kalman Filter, c) brick-wall filter, and d) Fermi filter. e) The mean residual and SNR of each fit shows that the Fermi filter yields the best result, as it is both the closest to the ideal pO_2 and presents the lowest noise.

**ADVANCED
SCIENCE NEWS**

www.advancedsciencenews.com

**ADVANCED
SENSOR
RESEARCH**
Open Access

www.advsensorres.com

excitation and collection optical filters, which are typically large (for wearable applications) and costly.

The combined effects of the developments introduced have significantly improved the sensitivity to changes in oxygenation within the physiological range (see Table S2, Supporting Information). The results of the human pilot study demonstrate the efficacy of this technology. By combining experimental characterization, calibration algorithms, and mathematical models,[32] reliable transcutaneous pO_2 readings can be obtained using our small, wearable TCOM sensors. Importantly, this can be achieved without the need for unrealistic conditions of constant temperature, humidity, or keeping patients immobile, which greatly expands the potential applications of this technology. The findings presented in this study have significant implications for the field of wearable technology and non-invasive oxygen monitoring. The improved TCOM wearable and the associated toolset provide a robust platform for obtaining accurate and reliable pO_2 measurements in real-world conditions. This advancement opens up opportunities for a wide range of applications, including clinical settings, sports physiology, and general health monitoring.

We note that the multilayer structure of the O_2-sensing film that was optimized can be set to reduce the diffusion of atmospheric oxygen into the film, resulting in a faster equilibration to the true tissue oxygen concentration. In principle, a totally impermeable layer would yield the best results in this sense, however for long-term wear applications,[38] water vapor must be allowed to partially diffuse out of the skin. Therefore, in order to create a wearable device that can continuously monitor for extended periods of time, a compromise has to be found between film permeability, sensitivity to tissue pO_2, and tissue health.

Future research can build upon these findings to further refine and expand the capabilities of this technology. For example, the optimized pO_2 metric can be improved by implementing an algorithm that detects motion artifacts. These could be detected via the addition of an accelerometer, or by searching for correlation within some sliding time window between the lifetime derived pO_2 (not prone to motion artifacts) with the intensity derived value. Finally, machine learning approaches could be very useful to achieve this goal,[28] and models could be trained with datasets containing calibration data in which motion has been added.

To conclude, in comparison with existing commercial TCOMs or devices found commercially or in the literature (see Table S1 Supporting Information), our device can present a simple, light, and inexpensive alternative to transcutaneous oxygen monitoring, thanks to the bright O_2 sensing phosphorescent metalloporphyrins on which it is based. The pilot study presented in this work demonstrates that the devices can reliably measure physiological changes in pO2 with a fraction of mmHg in precision, which is more than sufficient for the intended application. The calibration algorithms devised to address excitation source leakage present several advantages. First, they enable the differentiation of contributions to the measured phase from the excitation source from the dye, thereby enhancing the accuracy of the detected lifetime. Second, their implementation could potentially expand the scope of other wearables that rely on lifetime detection by reducing the demands on electronic components, allowing for the design of simple but reliable devices. Last, the applicability of these algorithms extends beyond their immediate context, offering potential use in phosphorescence-based sys-

tems in general. Specifically, the proposed algorithm could be useful in scenarios, where excitation signals interfere with final measurements, with the algorithm serving to eliminate such interference, enabling a more precise evaluation of luminescence lifetime across various applications.

Supporting Information

Supporting Information is available from the Wiley Online Library or from the author.

Conflict of Interest

The authors declare no conflict of interest.

Data Availability Statement

Research data are not shared.

[1] H. H. Moosa, M. S. Makaroun, A. B. Peitzman, D. L. Steed, M. W. Webster, *J. Surg. Res.* **1986**, *40*, 482.

[2] M. Vegfors, L. G. Lindberg, C. Lennmarken, *Acta Anaesthesiol. Scand.* **1992**, *36*, 346.

[3] N. R. Clay, C. M. Dent, *J. Bone Joint Surg. Br.* **1991**, *73*, 344.

[4] P. Abraham, Y. Gu, L. Guo, K. Kroeger, N. Ouedraogo, P. Wennberg, S. Henni, *Atherosclerosis* **2018**, *276*, 117.

[5] M. Stücker, P. Altmeyer, A. Struk, K. Hoffmann, L. Schulze, A. Röchling, D. W. Lübbers, *J. Invest. Dermatol.* **2000**, *114*, 533.

[6] M. Stücker, A. Struk, P. Altmeyer, M. Herde, H. Baumgärtl, D. W. Lübbers, *J. Physiol.* **2002**, *538*, 985.

[7] R. G. Tatevossian, C. C. Wo, G. C. Velmahos, D. Demetriades, W. C. Shoemaker, *Crit. Care Med.* **2000**, *28*, 2248.

[8] C. Koch, E. Chauve, S. Chaudru, A. Le Faucheur, V. Jaquinandi, G. Mahé, *Medicine* **2016**, *95*, 36.

[9] C. F. Poets, M. P. Samuels, J. P. Noyes, K. A. Jones, D. P. Southall, *Arch. Dis. Child.* **1991**, *66*, 676.

[10] G. Takahashi, I. Fatt, T. Goldstick, *J. Gen. Physiol.* **1966**, *50*, 317.

[11] M. Chen, H. J. Knox, Y. Tang, W. Liu, L. Nie, J. Chan, J. Yao, *Opt. Lett.* **2019**, *44*, 3773.

[12] S. Wang, R. Chen, Q. Yu, W. Huang, P. Lai, J. Tang, L. Nie, *ACS Appl. Mater. Interfaces* **2020**, *12*, 45796.

[13] W. Huang, R. Chen, Y. Peng, F. Duan, Y. Huang, W. Guo, X. Chen, L. Nie, *ACS Nano* **2019**, *13*, 9561.

[14] W. L. Rumsey, J. M. Vanderkooi, D. F. Wilson, *Science* **1988**, *241*, 1649.

[15] J. M. Vanderkooi, G. Maniara, T. J. Green, D. F. Wilson, *J. Biol. Chem.* **1987**, *262*, 5476.

[16] O. Stern, M. Volmer, *Phys. Z* **1919**, *20*, 183.

[17] M. F. Montero-Baker, K. Y. Au-Yeung, N. A. Wisniewski, S. Gamsey, L. Morelli-Alvarez, J. L. Mills, M. Campos, K. L. Helton, *J. Vascul. Surg.* **2015**, *61*, 1501.

[18] N. A. Wisniewski, S. P. Nichols, S. J. Gamsey, S. Pullins, K. Y. Au-Yeung, B. Klitzman, K. L. Helton, in *Oxygen Transport to Tissue XXXIX*, Springer, Berlin, Heidelberg **2017**, pp. 377–383.

[19] G. J. Kintz, W. A. McMillan, N. A. Wisniewski, Apparatus and methods for detecting optical signals from implanted sensors, **2019**, US Patent 10,219,729.

[20] Z. Yang, Implantable biosensor, **2005**, US Patent App. 10/631,908.

[21] C. J. Lim, S. Lee, J. H. Kim, H. J. Kil, Y. C. Kim, J. W. Park, *ACS Appl. Mater. Interfaces* **2018**, *10*, 41026.

[22] C.-J. Lim, J.-W. Park, *Sens. Actuators, A* **2019**, *298*, 111607.

[23] W. van Weteringen, T. G. Goos, T. van Essen, C. Ellenberger, J. Hayoz, R. C. de Jonge, I. K. Reiss, P. M. Schumacher, *Med. Biol. Eng. Comput.* **2020**, *58*, 239.

[24] Y. Katayama, Y. Fujioka, K. Tsukada, *IEEE J. Transl. Eng. Health Med.* **2020**, *8*, 1.

[25] I. Costanzo, D. Sen, J. Adegite, P. M. Rao, U. Guler, *IEEE Trans. Biomed. Circuits Syst.* **2021**, *15*, 474.

[26] V. Vakhter, B. Kahraman, G. Bu, F. Foroozan, U. Guler, *IEEE Trans. Biomed. Circuits Syst.* **2023**, *17*, 323.

[27] J. P. Cascales, E. Roussakis, L. Witthauer, A. Goss, X. Li, Y. Chen, H. L. Marks, C. L. Evans, *Biomed. Opt. Express* **2020**, *11*, 6989.

[28] J. P. Cascales, D. A. Greenfield, E. Roussakis, L. Witthauer, X. Li, A. Goss, C. L. Evans, *IEEE Internet Things J.* **2021**, *8*, 17557.

[29] E. Roussakis, Z. Li, N. H. Nowell, A. J. Nichols, C. L. Evans, *Angew. Chem., Int. Ed.* **2015**, *54*, 14728.

[30] E. Roussakis, J. P. Cascales, H. L. Marks, X. Li, M. Grinstaff, C. L. Evans, *Photochem. Photobiol.* **2020**, *96*, 373.

[31] G. A. Holst, T. Köster, E. Voges, D. W. Lübbers, *Sens. Actuators: B. Chem.* **1995**, *29*, 231.

[32] J. P. Cascales, A. E. Draghici, H. Keshishian, J. A. Taylor, C. L. Evans, *ACS Measurement Sci. Au* **2023**.

[33] J. O. Smith, *Introduction to digital filters: with audio applications*, vol. 2, W3K Publishing, **2007**.

[34] L. Witthauer, J. P. Cascales, E. Roussakis, X. Li, A. Goss, Y. Chen, C. L. Evans, *ACS Sens.* **2020**, *6*, 43.

[35] S. H. John W. Eaton, David Bateman, R. Wehbring, *GNU Octave version 3.8.1 manual: a high-level interactive language for numerical computations*, CreateSpace Independent Publishing Platform, **2014**, ISBN, 1441413006.

[36] J. P. Cascales, X. Li, E. Roussakis, C. L. Evans, *Biosensors* **2022**, *12*, 333.

[37] M. Müller, J. P. Cascales, H. L. Marks, M. Wang-Evers, D. Manstein, C. L. Evans, *ACS Sens.* **2022**, *7*, 3440.

[38] H. Marks, A. Bucknor, E. Roussakis, N. Nowell, P. Kamali, J. P. Cascales, D. Kazei, S. J. Lin, C. L. Evans, *Sci. Adv.* **2020**, *6*, eabd1061.